Chapter 7

MICROANGELO SCULPTING: WAVEGUIDE FABRICATION

7.1 Background

Waveguides are one of the fundamental building blocks of photonic circuits because they form the connections between all other optical components. In this chapter, we report the use of a thermocapillary sculpting technique which possesses the advantages of both smooth surfaces and large area patterning in a single process step. This technique has been named MicroAngelo and was discussed in Ch. 6 in relation to the fabrication of microlens arrays. We investigated the use of MicroAngelo to fabricate linear polymeric waveguides and characterized their physical and optical properties.

The remainder of this chapter is organized in the following manner. First, in Sec. 7.2 we briefly describe MicroAngelo and the fabrication process. Next, we characterize the fabricated waveguides physically, optically, and numerically in Sec. 7.3. We then discuss the particular advantages and disadvantages of fabricating linear waveguides with MicroAngelo in Sec. 7.4 and conclude with Sec. 7.5.

7.2 Thermocapillary Sculpting of Optical Waveguides

Thermocapillary forces have been the subject of scientific interest since the dawn of the 20th century and have garnered continued interest since then [62–64]. Thermocapillary forces are surface forces which arise in free surface films due to variations in surface tension caused by thermal gradients. Since surface tension is a generally decreasing function of temperature, warmer regions have a lower surface tension while cooler regions have a higher surface tension. This gradient in surface tension creates a shear along the interface from low to high surface tension which deforms the interface and with it, the bulk. During the past decade, attention has focused on the application of thermocapillary forces to molten nanofilms across which a temperature gradient is applied [1, 8–10, 39]. A typical experimental geometry is depicted in Fig. 7.1. An initially flat nanofilm with height h_o is heated from below and held at a temperature T_{Hot}. Concurrently, a cooled plate held at a temperature T_{Cold} is brought a distance d_o away from the hot plate. On this cool plate is a periodic, linear pattern defined photolithographically with height L_{pin}. In this study, the periodicity of the pattern was set so that neighboring waveguides would not

Figure 7.1: Schematic of the experimental setup used to fabricate waveguides

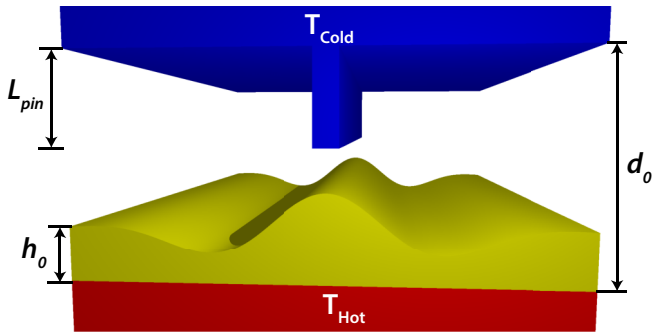

Schematic of the experimental setup (not to scale) which depicts the waveguide fabrication process. The molten nanofilm is bounded from below by a heated substrate and from above by a patterned linear mask which is actively cooled. The height of the pattern, L_{pin}, and the total plate separation, d_o, are typically on the order of microns, while the initial film thickness, h_o, is on the order of hundreds of nanometers. Note that only one line in the pattern is shown in this figure, but the patterns used in the study were periodic laterally on the order of 500 microns.

interact (periodicity of 500 μm or larger). The width of the protruding lines in the pattern was equal to 3 μm. The presence of the pattern localizes the thermocapillary stress beneath it and causes local deformation upwards which produces the desired waveguides. We note that the temperatures set for the heater, T_{Heater}, and the chiller, $T_{Chiller}$, are not equal to T_{Hot} and T_{Cold}, respectively, due to temperature drops within the setup itself.

The details of the heating and cooling in the experimental setup used in the this study have been described previously in Ch. 6. As such, we will only briefly outline the waveguide fabrication procedure here and highlight the differences in the patterned mask. The waveguide material was chosen to be polystyrene (PS) and the substrate was 5 micron thick thermal silicon dioxide on a silicon wafer (WRS Materials). PS is a commonly used polymer for optical devices because it has low optical absorption [65] and is readily available commercially [66]. The substrate material was chosen because the oxide has a lower refractive index than the PS which is a requirement for guided modes to exist in the PS layer. The wafer was also very flat, which allowed for precise fabrication and then for the underlying silicon wafer to be cleaved to produce coupling facets and to isolate the waveguides. To create the initially flat nanofilm, PS was dissolved in toluene at 3% to 6% weight and then spun coat on the oxide wafers at 2000 to 3000 RPM for 30 seconds with an acceleration of 1000 RPM/s. The toluene rapidly evaporated, which left a thin solid film of PS which was suitable for waveguide fabrication. The solid nanofilm was inserted into the experimental setup and brought into contact with patterned spacers on the top plate

Table 7.1: Experimental parameters for each of the four fabricated waveguides

Sample Number	1	2	3	4
h_o (nm)	164	147	138	223
d_o (μm)	10.7	10.7	10.7	10.3
L_{pin} (μm)	4.29	4.29	4.29	3.34
T_{Heater} (°C)	120	120	120	150
T_{Chiller} (°C)	30	30	30	40
t (min)	10	15	45	265

(not shown in Fig. 7.1) which set the total gap distance, d_o, to around 10 microns. The previously fabricated patterns had heights of L_{pin} ranging from 3.34 to 4.29 μm. A full listing of the experimental parameters for the waveguides presented in this study can be found in Table 7.1. As compared to the mask patterns in Ch. 6, these patterns are linear and show periodicity in only one direction whereas the patterns for MLA fabrication had 2D periodicity. The film was heated for times between 10 minutes and 4 hours at heater temperatures of 120 to 150 °C with an external chiller setpoint of 30 to 40 °C. After the fabrication period, the sample was allowed to cool back to the temperature of the chiller which occurred within 10 to 15 minutes. At this point, the waveguides had solidified and were removed from the experimental setup. After visual inspection to locate the waveguides, the silicon wafer was cleaved to isolate the fabricated waveguides and produce high quality end facets suitable for optical coupling.

7.3 Waveguide Characterization

We undertook an extensive study of the linear waveguides and their physical and optical properties. Physical characterization was accomplished using optical microscopy, coherence scanning interferometry, and profilometry to inspect the waveguide surface and extract the profile of its cross section. The optical characterization focused on measurement of the number of waveguide modes, the structure of those modes, a lower bound on the coupling efficiency, and the TM extinction ratio for those waveguides which supported only TE modes. Numerical simulations were also performed to compute the waveguide mode structure and compared with the experimental results.

Figure 7.2: Images of a fabricated waveguide

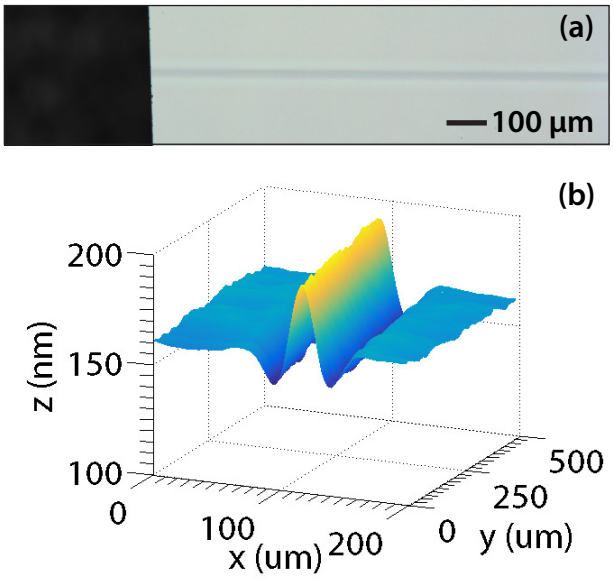

(a) Optical microscope image of a waveguide seen from above. The underlying substrate has been cleaved to produce the sharp facet seen on the left. (b) Coherence scanning interferometry data of the waveguide surface.

7.3.1 Physical Characterization of Waveguides

After cleaving, the waveguide structure was first visually inspected with an optical microscope for any large scale defects which interacted with the waveguide backbone. A representative image of the waveguide seen from above is shown in Fig. 7.2(a). The cleaved edge shows a sharp transition at the end facet with no rounding or deformation of the waveguide facet. The backbone of the waveguide is visible as a slightly darker horizontal stripe in this image due to thin film interference. The waveguide surface profile was then analyzed with a coherence scanning interferometer (Zemetrics ZeGage). One such surface profile scan is shown in Fig. 7.2(b).

Additionally, the waveguide cross section was measured with a profilometer (Dektak XT) in the direction perpendicular to the direction of light propagation within the waveguide. For the waveguide shown in Fig. 7.2(a), this corresponds to a scan in the vertical direction and four such scans are plotted in Fig. 7.3. The profile of the waveguide cross section was then fit by an analytic function so that it could be used in the numerical simulations described below. The fitting function for this structure was a sinusoid modulated by a Gaussian decay. All of the profilometer data was shifted so that the peak of the waveguide occurred at $x = 0$, which allowed us to use

Figure 7.3: Profilometer scans of waveguide cross sections

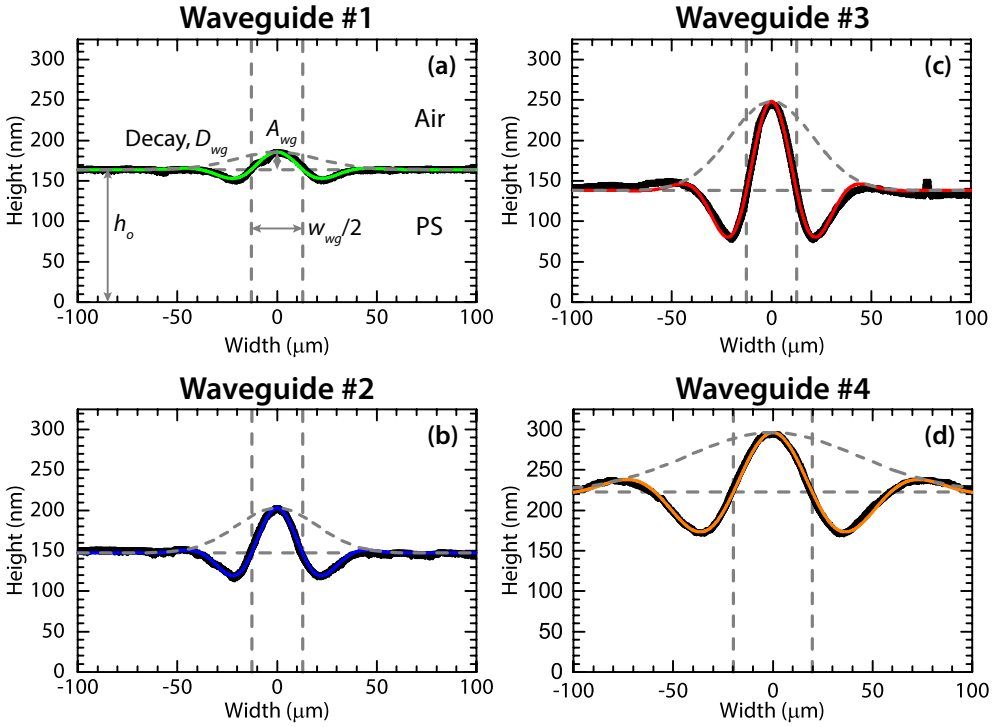

Profilometer cross sections of four waveguides perpendicular to the propagation direction. In the optical image from Fig. 7.2(a), this corresponds to a scan in the vertical direction. The solid curves are numerical fits parameterized by Eq. 7.1 and the numeric values of the constants can be be found in the third column of Table 7.2. The waveguide shown in Fig. 7.2 corresponds to the profilometer scan in (b).

a simple sinusoid without a lateral offset. The function had the form

$$F(x) = A_{wg} \cos\left(\frac{2\pi x}{w_{wg}}\right) e^{-(x/D_{wg})^2} + h_o, \tag{7.1}$$

where A_{wg} is the amplitude of the waveguide, w_{wg} is the waveguide width, D_{wg} is the decay of the Gaussian, and h_o is the background film height, which was equal to the initial film thickness of the solid nanofilm. A full listing of the fits for the waveguides considered in this study can be found in Table 7.2.

7.3.2 Optical Waveguide Modes

As seen in Fig. 7.3, the resulting waveguide cross section is very different from a traditional rectangular waveguide cross section produced from photolithographic techniques. As such, the structure of the waveguide modes is of interest here. To couple light into the MicroAngelo waveguides, we used a setup which is diagrammed

Table 7.2: Fitting constants for the measured waveguide cross sections for each of the waveguides

Sample Number	1	2	3	4
A_{wg} (nm)	22	56	110	73
w_{wg} (μm)	51	51	50	79
D_{wg} (μm)	29	29	29	61
h_o (nm)	164	147	138	223

Figure 7.4: Diagram of optical characterization setup

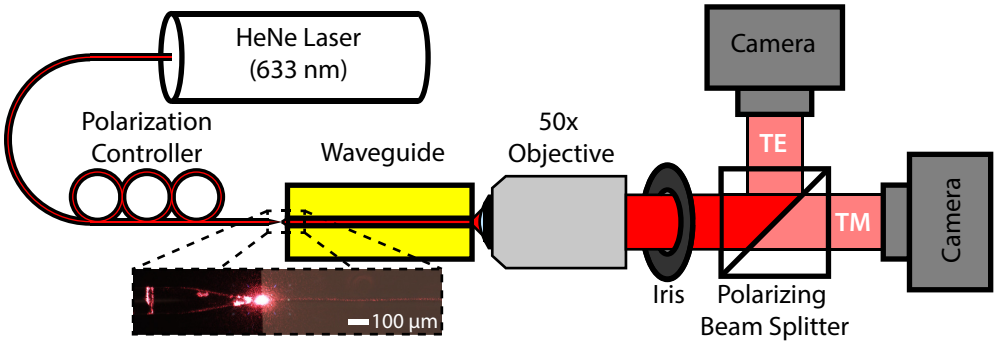

Diagram of the optical testing setup which allows for coupling of light into the waveguide modes and then visualization of the waveguide output. The waveguide modes are visualized simultaneously in both TE and TM polarizations through the use of a polarizing beam splitter (PBS).

in Fig. 7.4. Light from a HeNe laser (Meller Optics, 25-LHP-991-249, 633 nm) was coupled into a lensed single mode optical fiber (Lase Optics LF-SM-DW-07-630-HP-FC/APC, 500 nm x 10 μm spot size, 50°wedge angle) which was end coupled to the waveguide. This fiber was mounted on a stages which provided three translational degrees of motion as well as tip, tilt, and rotation control. After the sample was mounted on a separate stage with three translational degrees of freedom, the output facet of the waveguide was brought to the focal plane of a 50x microscope objective. The image of the microscope objective was focused concurrently on two cameras after passing through an iris and a polarizing beam splitter (Thorlabs PBS25-633). The iris was adjusted so that the only light which corresponded to the guided mode passed through. This reduced background scattered light from defects and cladding modes (when they exist). In addition to the polarization separation achieved by the beam splitter, the polarization of the input light was controlled through the use of a polarization controller (Thorlabs FPC030).

Generally, we have presented one waveguide from each of four different regimes in Table 7.2, starting from the smallest and proceeding to the largest waveguides. The smallest waveguide was single mode with only a single TE mode. The next smallest waveguide had several TE modes, but no TM modes. The third waveguide in the table had a few TM modes and many TE modes. The last, and largest, waveguide had many TE and many TM modes. The qualitative features of waveguide #1 and #2 are similar, as are #3 and #4. As such, we will only present coupling images for waveguides #2 and #3.

Waveguide #2 is the second smallest waveguide presented, (second column in Tables 7.1 and 7.2) and has several TE modes and these are shown in the left column of Fig. 7.5. Interestingly, no TM modes were observed for this waveguide. The different TE modes were selectively excited by moving the lensed optical fiber laterally along the input facet of the waveguide. The first order mode could be found in the middle of the waveguide and then small translations in either direction yielded successively higher order modes in sequential order. Looking closely at the higher order modes in Fig. 7.5(b) and (c) there is a slight asymmetry in the mode profile. We ascribe this to the fact that the coupling was dominated by the higher order mode but that there were still some lower order mode excitations which were localized on the side which the fiber was translated towards. For the higher order modes with multiple lobes, the image was normalized to the less intense lobe to highlight the structure. In general, we observed that the lateral extent of the mode increased as the mode order did. The vertical confinement was good at all mode orders although the exterior lobes of the higher order modes extended successively further into the silicon dioxide layer.

If we increase the dimensions of the waveguide, as in waveguide #3 (third column of Tables 7.1 and 7.2) the waveguide can then support TM modes. The images in Fig. 7.6 show the only two TM modes of waveguide #3. Generally, a modest number of modes of either polarization were easy to identify and selectively excite by moving the coupling fiber. Once there are many modes, as is the case for the TE modes of waveguide #3 and #4, it becomes difficult to definitively selectively excite and categorize them. This is especially true when simultaneously exciting TE and TM modes because the fiber position which excited a clean TM mode often excited multiple TE modes, and vice versa. As such, we have not presented TE modes for waveguide #3, although they do exist and are qualitatively similar to the TE modes presented in Fig. 7.5. No attempt was made to optimize and match the modes of the

Figure 7.5: Optical images of the TE modes from waveguide #2

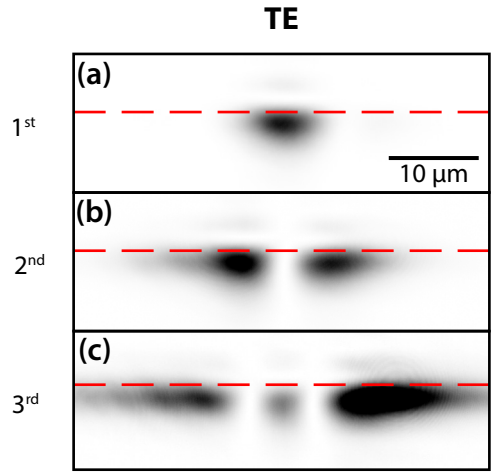

Optical images of the TE modes from a μAngelo waveguide. Each mode has been normalized to show the mode structure. The thickness of the PS film is approximately 100 nm to 200 nm and the dotted line is the presumed film location. Both the vertical and horizontal scales are equal.

Figure 7.6: Optical images of the TM modes from waveguide #3

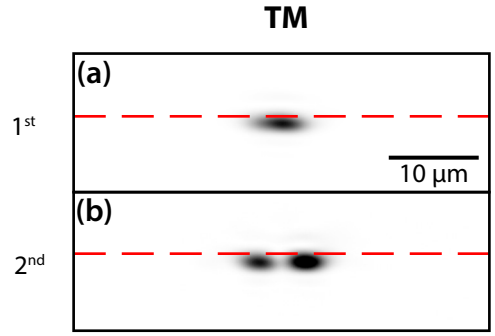

Optical images of the TM modes from a μAngelo waveguide. Each mode has been normalized to show the mode structure. The thickness of the PS film is approximately 100 nm to 200 nm and the dotted line is the presumed film location. Both the vertical and horizontal scales are equal.

fiber to the modes of the waveguides in this study.

Beyond the qualitative observations of the mode structure, this optical setup has the capability to quantitatively measure two aspects of the waveguides: a lower bound on the coupling efficiency and the TM extinction ratio. By replacing the cameras with photodiodes, the power of both the TE and TM polarizations was measured concurrently. In this configuration, the coupling efficiency was measured by normalizing the measured power in each photodiode when the waveguide was inserted by the measured power when the waveguide was not present and the optical fiber was at the focal point of the imaging objective. This measurement quantifies

Table 7.3: Coupling efficiency lower bounds and TM extinction ratio measurements

Sample Number	1	2
TE Coupling Efficiency Lower Bound (%)	2.4	16
TM Extinction Ratio (dB)	-36	-36

the amount of incident power which the waveguide transmitted, although it is only a lower bound because we did not optimize the mode matching between the coupling fiber and the waveguide. For the waveguides that only support TE modes, they can be used as polarizing waveguides in the same vein as in-line polarizers. It is therefore interesting to characterize the TM extinction ratio of the waveguides. Note that this measurement only applies to those waveguides which do not support TM modes. This measurement was completed by taking the ratio of the coupling efficiencies for the TM and TE modes for a given coupling position. In other contexts, this number is often computed by taking the ratio of the optical powers which pass through the waveguide or polarizer. This would be equivalent to the procedure described above if the amount of power in both the TE and TM modes was equal. However, MicroAngelo waveguides which only have TE modes are so efficient at damping optical power in the TM polarization that we must put significantly more TM power than TE power into the waveguide to have a measurable TM signal. As a result, the use of coupling efficiencies instead of raw optical powers compensates for the fact that the input power in each polarization was not equal. This technique relies on the assumption that the coupling for the TE and TM modes was equal, which will only strictly hold for the lowest order mode. As such, the coupling efficiency lower bounds and TM extinction ratio results for only the lowest order modes are listed in Table 7.3. We note that these extinction ratio measurements are pushing the limits of the experimental setup because the PBS is only listed to -35 dB. Additionally, this large extinction ratio was expected because this sample did not support TM modes.

7.3.3 Numerical Simulations of Waveguide Properties

Because of the special profile of the waveguides, it is important to understand the mode structure in the waveguide. Since the waveguide geometry described by Eq. (7.1) was too complicated to solve analytically for the waveguide modes we performed numerical simulations to investigate the number of modes, mode structure, and the effective refractive index of the modes. The finite element simulations

were performed using commercial software [28] to simulate the wave equation and the geometry of the simulations is diagrammed in Fig. 7.7(a). The overall domain measured 100 microns in width and 10 microns in height. The lower half of the domain was thermal oxide with refractive index 1.457 [67] (at λ_{opt} = 633 nm) and the waveguide surface was defined using Eq. (7.1) and the geometric parameters in Table 7.2. The PS was modeled with a refractive index of 1.58, which was measured by an Abbe refractometer (Vee Gee Instrubments C10); see Appendix A.6 for more details about this instrument. The remainder of the geometry was an air domain with a refractive index of 1.0001. The exterior boundaries of the domain were modeled as perfect electric conductors, although the exterior boundaries were positioned far enough away from the modes that the specific choice of boundary condition had virtually no effect on the calculated modes. The domain was meshed with mapped rectangular elements. Five elements composed the height of the waveguide and 32 elements were used in the vertical direction for the two domains above and below the waveguide. In the lateral direction, 2500 elements were used which kept the shape of the elements within the waveguide nearly square and smaller than $\lambda_{opt}/4$. In total, 170,000 elements were used with approximately 2×10^6 degrees of freedom. The geometry of the simulated waveguide is shown in Fig. 7.7(a) using the the waveguide geometries listed in Table 7.2. In Fig. 7.7, the numerical simulations of the modes corresponding to Figs. 7.5 and 7.6 are shown. Each mode is normalized to have unit intensity for presentation purposes and there is qualitative agreement between the simulated modes and the experimental modes presented previously.

Comparison of μAngelo Waveguides to Rectangular Waveguides

Waveguides fabricated lithographically typically have rectangular cross sections while MicroAngelo waveguides do not as Fig. 7.3 clearly demonstrates. As such, this difference in cross section is a natural comparison point for MicroAngelo waveguides. We have compared the mode structure of waveguides with a rectangular cross section to MicroAngelo waveguides in Fig. 7.8. The computational geometry for the rectangular waveguides is shown in Fig. 7.8(a). The geometric parameters of the rectangular waveguide were equivalent to those used in Fig. 7.7(a), although the decay parameter of the Gaussian, D, is not needed. For the purposes of this comparison, we chose to use the largest waveguide presented in the fourth column of Table 7.2. In Fig. 7.8(b) and 7.8(c) the intensity of the first 10 TE modes have been plotted as a function of lateral position. Each successive mode has been normalized to unity and offset vertically for visualization. These curves are produced

Figure 7.7: Computational domain and simulated waveguide modes

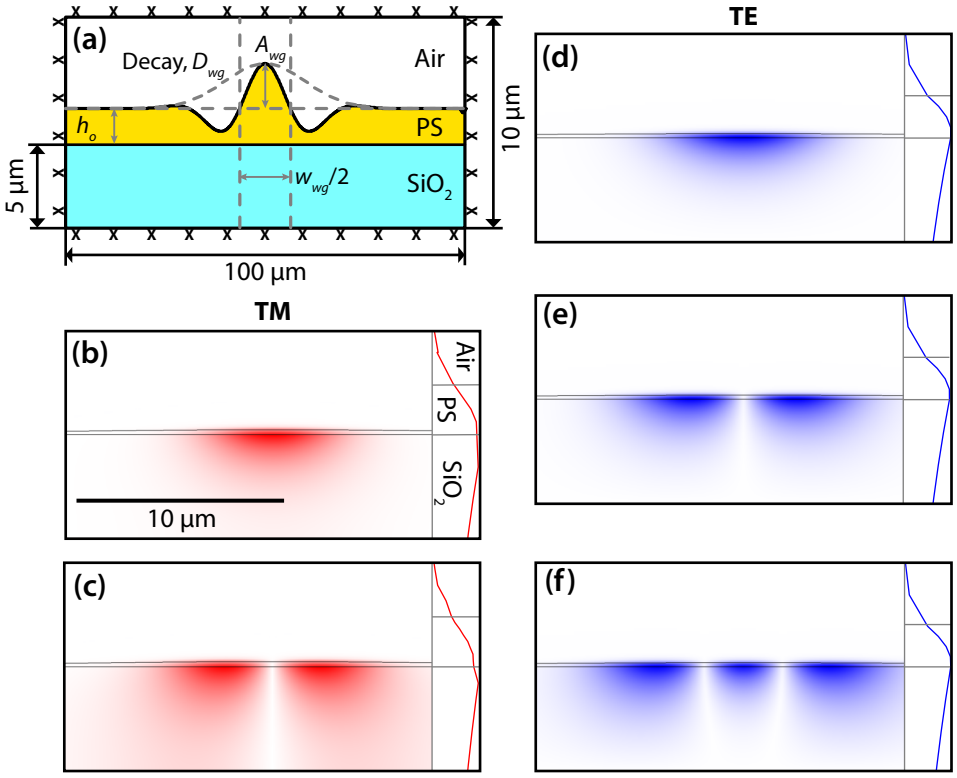

(a) Schematic of the domain (not to scale) used in the finite element simulations of the μAngelo waveguide modes. The overall domain is centered on the waveguide maximum whose analytic form was determined by fitting a profilometry scan of the waveguide cross section, as in Fig. 7.2(c). The boundary condition on all sides was a perfect electric conductor condition. (b), (c) Simulated TM modes for waveguide #3 which possessed two TM modes and whose experimentally measured modes were shown in Fig. 7.6. (d), (e), (f) Simulated TE modes for waveguide #2 whose experimentally measured modes were shown in Fig. 7.6. For all parts (b) through (f), the curves on the right show a magnified plot of the E-field magnitude through the three material layers at the lateral location of maximum intensity.

by integrating the mode structure, such as those shown in Fig. 7.7(b) and 7.7(c), in the vertical direction. In addition, the lateral extent of the rectangular waveguide has been added to Fig. 7.8(b) to highlight the fact that modes of every order extend over the entire cross section of the waveguide. In Fig. 7.8(c) the overlaid parabola does not correspond to the physical waveguide cross section, but is to help guide the eye and highlight the fact that higher order modes in MicroAngelo waveguides have larger lateral extent. Additionally, these two plots spur an analogy to quantum mechanics. The modes of the rectangular cross section waveguide in Fig. 7.8(b) bear a striking resemblance to the modes of the infinite square well. Similarly, the modes in Fig. 7.8(c) for a MicroAngelo waveguide bear a strong resemblance to the modes of the quantum harmonic oscillator. This implies that the mode structure of

the waveguides is analogous to the probability density of the wavefunction in the corresponding quantum system. Furthering this analogy we can also associate the eigenvalues of each problem so that the effective refractive index of the waveguide modes would be analogous to the energy of the corresponding quantum system. This analogy would imply that the same relationships hold between the energy differences of consecutive modes and the difference between the effective refractive index of consecutive modes. The energy difference between consecutive modes in the quantum harmonic oscillator is [68]

$$E_{\nu+1} - E_\nu = \hbar\omega \propto \text{Constant}, \tag{7.2}$$

where $\hbar$ is the reduced Planck's constant, ω is the frequency of the oscillator, and ν is the mode order. For the infinite square well, the energy difference between modes is

$$E_{\nu+1} - E_\nu = \frac{\hbar^2\pi^2\,(2\nu+1)}{2ma^2} \propto \text{Linear}. \tag{7.3}$$

In this expression, m is the mass, and a is the width of the well. Based on these results, we would expect that the difference between the effective refractive index of consecutive modes for the waveguide with a rectangular cross section should be linear in the mode number, while for MicroAngelo waveguides, the difference should be constant. As plotted in Fig. 7.8(d), the effective refractive index differences do indeed follow this trend for the first 10 modes. The trend continues until close to cutoff where the effective refractive index of the waveguide modes is very close to the refractive index of the cladding.

Single Mode μAngelo Waveguides

With a better understanding of how the waveguides studied in this work compare to traditional waveguides with rectangular cross sections, we investigated another major criteria for waveguide fabrication. The ability to create single mode waveguides is a crucial benchmark for future photonic circuits created with MicroAngelo because single mode waveguides are much easier to work with than multi-mode waveguides. All traditional lithographic techniques are able to make single mode waveguides and we have successfully fabricated a single mode waveguide with MicroAngelo. The dimensions of this waveguide are in the first column of Table 7.2 and we observed only a single TE mode which was quite similar to the first order mode shown in

Figure 7.8: Comparison between MicroAngelo and rectangular waveguides

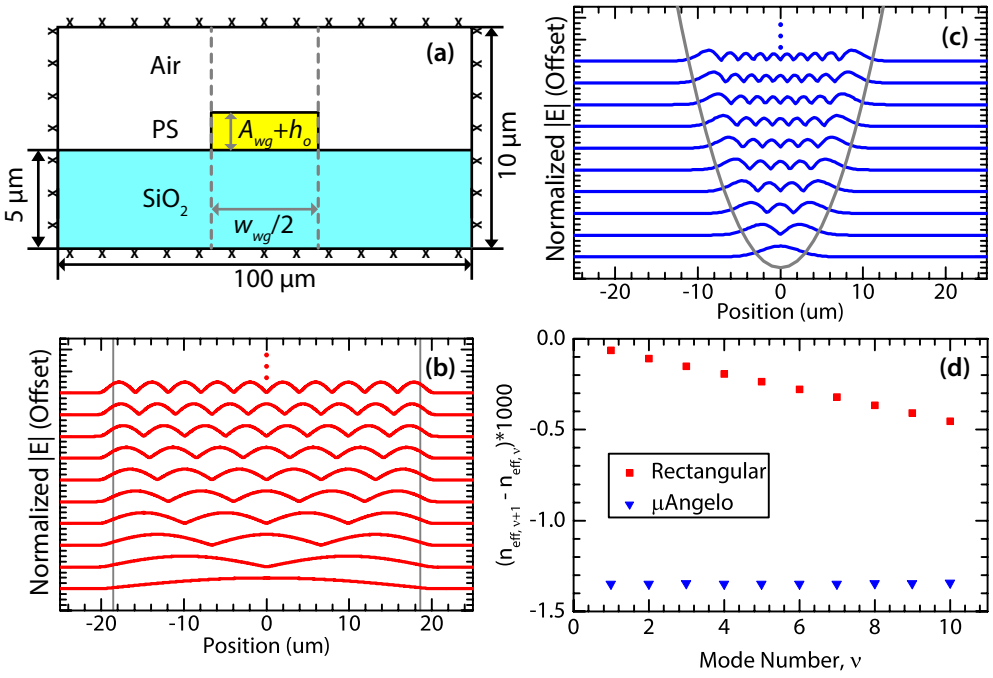

(a) Schematic of the domain (not to scale) used in the finite element simulations of the rectangular waveguide modes. The same waveguide dimensions are used to parameterize the rectangular geometry as in Fig. 7.7(a). The boundary conditions on the exterior edges of the domain are all perfect electric conductors. (b) Spatial distribution of waveguide mode intensity of a rectangular waveguide with the dimensions listed in the fourth column of Table 7.2. The vertical lines in this plot denote the edges of the rectangular waveguide. (c) Spatial distribution of waveguide mode intensity for a μAngelo waveguide with the dimensions listed in the fourth column of Table 7.2. The overlaid parabola in this plot does not correspond to the waveguide surface profile, it is solely to guide the eye. (d) Effective refractive index difference between successive modes plotted as a function of mode number for both rectangular and μAngelo waveguides.

Fig. 7.5(a). Generally, there are two ways to achieve single mode operation. The first is to tune the geometry to only support a single mode at a specified wavelength. The second is to tune the wavelength for a given geometry. We considered both of these scenarios in turn using numerical simulations to vary the relevant parameters.

To investigate the effect of geometry on the number of waveguide modes, we performed a numerical parameter sweep in which three parameters of the fitting function defined by Eq. 7.1 were varied. In particular, we varied the waveguide width, w_{wg}, the background film height, h_o, and the waveguide amplitude, A_{wg}. In a separate scan (not shown here), we also varied the Gaussian decay, D_{wg}, but found that it did not have an appreciable effect on the number of guided modes in the parameter regime where we have fabricated waveguides. The wavelength for this computational study was held fixed at 633 nm to match the experimental setup. The results of

the parameter sweep are plotted in Fig. 7.9(a) where we varied the waveguide width from 45 to 80 microns in steps of 5 microns. Simultaneously, the amplitude was varied from 5 to 160 nanometers in steps of 5 nanometers while the background film height was varied from 100 to 170 nanometers also in steps of 5 nanometers. Each point on this graph represents a set of geometric parameters which only supports a single TE mode. After completing this scan, we noted that the amplitude and the background film height are strongly correlated and so we have plotted this same data set in Fig. 7.9(b) where the waveguide width is plotted against the total waveguide height which was defined as $A_{wg} + h_o$. Based on these results, there is a clear region of parameter space where single mode waveguides can be fabricated, but that the tolerances on each of the geometric parameters, besides D_{wg}, are relatively strict.

Instead of varying the geometry as was done in Fig. 7.9, the geometry can be held fixed and the wavelength of the guiding light varied. In this way, a waveguide with a fixed geometry should be single mode for some range of wavelengths. For these simulations, the geometry of waveguide #2 was used while the wavelength was varied. The wavelength was varied from 550 nm to 750 nm in steps of 5 nm and over this range the refractive indices of the PS and the thermal oxide have significant variation. For this study, we used the refractive index values as a function of wavelength for silicon dioxide from literature [67], while for PS we used the Cauchy equation whose coefficients were determined from a set of three independent measurements made at different wavelengths using an Abbe refractometer (see Appendix A.6 for more details). The results of this wavelength scan are plotted in Fig. 7.10. There is a large range spanning over 100 nm in wavelength for which this waveguide geometry will support TE modes, but will not support TM modes. This is called the polarization window and MicroAngelo waveguides have polarization windows greater than 100 nm which is competitive with commercial polarizing optical fibers [69]. Furthermore, there is a 30 nm window in wavelength near 750 nm where this geometry will be single mode.

7.4 Discussion of MicroAngelo Waveguides

There are several unique features related to fabricating waveguides with MicroAngelo. First, the surfaces are solidified directly from a melt. As such, they have minimal surface roughness which means that there are minimal scattering losses from the waveguide surface. Second, the most unique property of the technique is that it can fabricate curved optical structures which would be difficult or time consuming with traditional techniques. Due to conservation of mass, the waveguide

Figure 7.9: Single mode MicroAngelo waveguide geometries

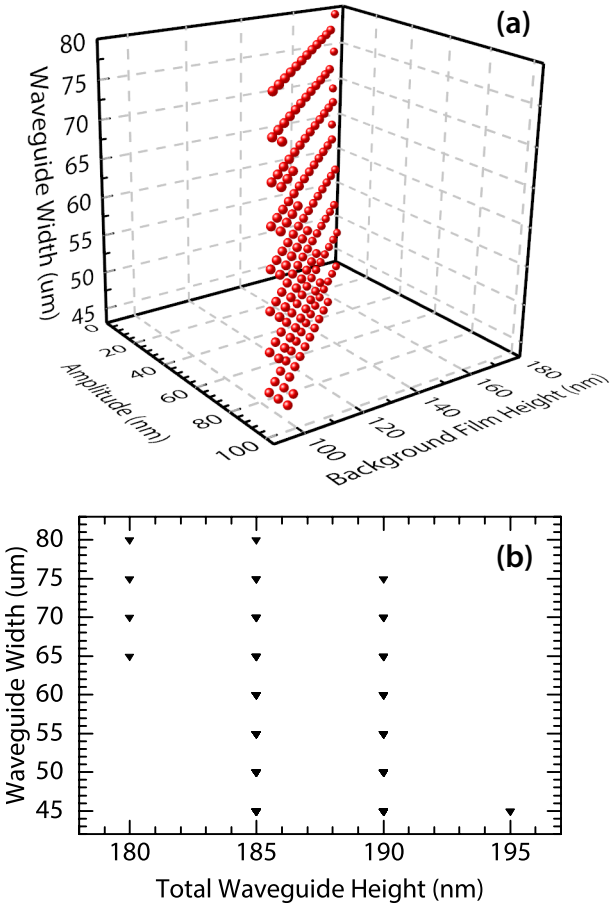

(a) Numerical parameter sweep of the waveguide dimensions to determine the geometries which would support only a single guided mode. These parameter ranges incorporate the full range of waveguides which have been fabricated to date. The value of the decay was fixed at 29 μm and variation of it was found to have negligible impact on the number of guided modes. (b) Single mode geometries as a function of waveguide width, w, and total waveguide height, $A_{wg} + h_o$.

formation process depletes the immediately adjacent regions which leads to a self-localizing effect. Third, MicroAngelo is a parallel fabrication technique which can pattern large areas simultaneously. This means that it is fast, efficient, and scalable.

On the other hand, MicroAngelo is restricted to the long wavelength regime. This means that the fabricated structures will always have relatively flat profiles, with small aspect ratios (height:width), which leads to strong geometric birefringence. Due to the vastly different length scales in the lateral and vertical directions, the TE polarization is strongly preferred over the TM polarization. This causes the polarizing behavior of waveguides 1 and 2 in Table 7.2 and the polarization window in Fig. 7.10. It is also interesting to note that single mode waveguide operation

Figure 7.10: Polarization window of waveguide #2

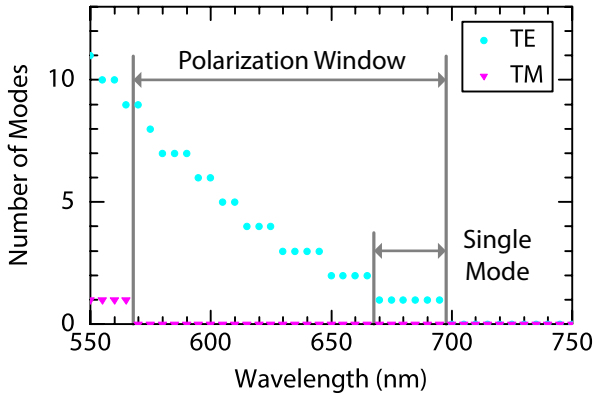

Number of guided modes as a function of the wavelength of light which is being guided. There is a significant region where the waveguide functions as a polarizing waveguide since it supports TE modes but not TM modes. Additionally, a subset of this region supports only a single TE mode.

in this case is truly single mode in the sense that there is only one mode with TE polarization. Most single mode waveguides support one mode in each of the two orthogonal polarizations, TE and TM.

The strong geometric birefringence in waveguides created by the small aspect ratio is not solely restricted to waveguides fabricated with MicroAngelo. For instance, a rectangular waveguide which has a small height and a large width would show similar effects [70]. What is unique about the nonrectangular cross sections of these waveguides is that they localize the modes near the center of the waveguide. This mitigates the difficulties associated with coupling from an optical fiber into the waveguide modes. From a practical perspective, this means that you can get the unique polarization characteristics in a MicroAngelo waveguide with far less of a decrease in coupling efficiency as compared to an equivalent rectangular waveguide.

The ability of these waveguides to act as polarizing elements means that they can be integrated natively onto a chip and function as useful optical elements without the need for a polarization splitter or rotator. Additionally, we have shown that they possess characteristics comparable to commercial alternatives but with a much smaller footprint. This work on linear waveguides has also laid the foundation for the fabrication of more complex optical components which could be fabricated with MicroAngelo. In the future, these optical components could be integrated into optical photonic circuits which can be fabricated in a single process step.

7.5 Summary

In this chapter, we have demonstrated the capability of thermocapillary sculpting to fabricate linear optical waveguides out of polymeric nanofilms. We extensively characterized their physical characteristics and optical properties. We identified the unique properties of these waveguides. In particular, the very small aspect ratio of the waveguides induced geometric birefringence which preferentially suppressed the TM modes in favor of TE modes. Due to the nonrectangular cross section of the waveguide, the modes were localized near the center of the waveguide which allowed us to couple to them more effectively than would have been otherwise possible. The waveguide mode structure observed experimentally showed qualitative agreement with the numerical simulations. Furthermore, we performed numerical parameter sweeps to investigate geometries and wavelengths where these waveguides would support only a single guided TE mode. The fabrication process and unique waveguide properties open new possibilities in integrated photonic circuits and sensor applications.